Measurements of X-ray Imaging Performance of Granular Phosphors With Direct-Coupled CMOS Sensors

Min Kook Cho, *Student Member, IEEE*, Ho Kyung Kim, *Member, IEEE*, Thorsten Graeve, Seung Man Yun, Chang Hwy Lim, Hyosung Cho, and Jung-Min Kim

Abstract—For Gd_2O_2S:Tb granular phosphor screens having a wide range of mass thicknesses, we have investigated the fundamental imaging performance in terms of modulation-transfer function (MTF), noise-power spectrum (NPS) and detective quantum efficiency (DQE). As an optical photon readout device, a CMOS photodiode array with a pitch of 48 μm was used. Under the representative radiation quality, RQA 5, recommended by the IEC (International Electrotechnical Commission, Report 1267), the MTF was measured using a slanted-slit method to avoid aliasing and the NPS was determined by two-dimensional (2D) Fourier analysis of white images. The DQE was assessed from the measured MTF, NPS and the estimated photon fluence. Figure-of-merit (FOM) curves are presented to describe the tradeoff between the X-ray sensitivity and spatial resolution of screens as a function of mass thickness. This study will be useful for the selection guidance of Gd_2O_2S:Tb phosphors for the relevant imaging tasks of digital radiography.

Index Terms—Detective quantum efficiency, digital radiography, granular phosphor, modulation-transfer function, noise-power spectrum.

I. INTRODUCTION

RECENT microelectronic technologies in the flat-panel display industry and the digital camera business have led to the digitalization of medical X-ray imaging. For digital X-ray imaging, the amorphous silicon-based pixel matrix and the charge-coupled device (CCD) are in the spotlight because of their intrinsic capabilities of two-dimensional (2D) imaging and well-known technologies [1]. The CMOS (complementary metal-oxide-semiconductor) sensor has also lately attracted considerable attention [2], [3].

The terbium-doped gadolinium oxysulfide $(Gd_2O_2S$:Tb$)$ granular phosphor screen is the most popular X-ray converter,

and often employed in digital radiographic imaging systems owing to its well-known technology and ease of handling in size, thickness, and flexibility [2], [4]–[6]. Furthermore, it is very cost-effective. Thallium-doped cesium iodide (CsI:Tl) with columnar structure has recently received much attention because of the great spectral matching to a readout pixel array and its high spatial resolution [7].

Various imaging tasks and applications necessitate careful selection and design of the scintillator in terms of its sensitivity and spatial resolution. In this study, we have investigated the fundamental imaging performance of Gd_2O_2S:Tb phosphor screens in terms of modulation-transfer function (MTF), noise-power spectrum (NPS), and detective quantum efficiency (DQE). The measurements have been performed based on the guidelines published by the International Electrotechnical Commission (IEC) [8], which has standardized the methodology for measuring DQE in a digital detector.

Other, similar studies of imaging properties of various scintillators have been described in the literature [9]–[12], but that this is one of the first detailed studies with a direct-coupled CMOS sensor.

II. MATERIALS AND METHODS

A. Sample Phosphor Screens

Commercially available Gd_2O_2S:Tb screens with various mass thicknesses (Eastman Kodak, Rochester, NY) were prepared to be investigated. The mass thickness is the weight of phosphor coated per unit area. The specifications of samples are summarized in Table I [5], [13]. Illustration of the screen structure, for example, Lanex™ Fast Back is as follows [13]. A schematic illustration of the Lanex™ Fast Back screen is shown in Fig. 1. The screen has an overcoat which is about 13-μm-thick. The phosphor layer is about 300-μm-thick and is coated onto a polyester support which is about 175-μm-thick. The support contains TiO_2 to provide a reflectance of about 88% at the 545 nm emission of the phosphor. A certain type of screen such as Lanex™ Fine has no reflector, thus maximizing the spatial resolution. On the back of the support is an anti-curl layer which keeps the screen flat. This layer is about 50–60-μm-thick. The phosphor layer is made up of Gd_2O_2S:Tb as the phosphor. The binder is a polyurethane elastomer. The aimed mass thickness of the Lanex™ Fast Back is ~ 135 mg/cm³. The phosphor density is 7.3 g/cm³.

As described in Table I, the mass thickness of the phosphor layer is the main variable determining the screen speed and the
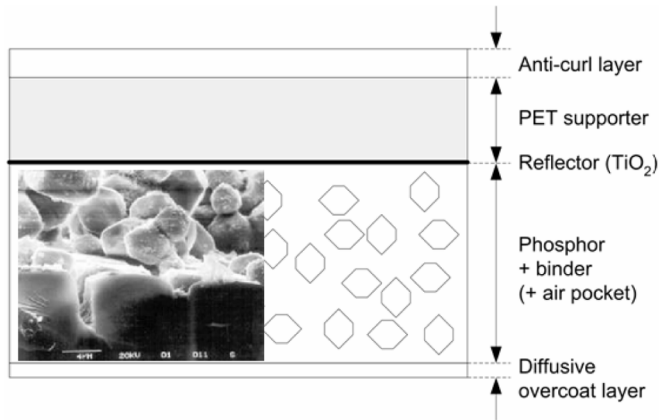
Fig. 1. Schematic illustration of the Lanex™ Fast Back screen. The detailed descriptions are given in the text and Table I.

TABLE I
SUMMARY OF SCREEN SPECIFICATIONS

Screen types	Physical parameters		
	Mass thickness (mg/cm^2)	Thickness (μm)	Density ^{a} (g/cm^3)
Min-R™	33.91	90	3.77
Min-R™ 2000	33.91	84	4.04
Min-R™ 2190	33.91	85	3.99
Lanex™ Medium	59.20	160	3.70
Lanex™ Fast Front	48.44	110	4.40
Lanex™ Fast Back	134.55	300	4.48

^{a} Estimation based on the given mass thicknesses and thicknesses.

spatial resolution. It is noted that the density was calculated based on the given mass thicknesses and approximate thicknesses.

B. Experimental Setup and Imaging Conditions

For the X-ray irradiation, an X-ray tube having a rotating tungsten anode (E7239X, Toshiba, Japan) was used. The inherent filtration due to the internal tube structures and the glass of the beam collimator is 2.4 mm in aluminum equivalent.

As a readout device of optical photons emitted from the overlying Gd_2O_2S:Tb screens, a CMOS photodiode pixel array (RadEye™, Rad-icon Imaging Corp., USA) [14] was employed. The CMOS photodiode array has a format of 512×1024 pixels with a pitch of 48 μm. The Gd_2O_2S:Tb screen was directly overlaid onto the active area of the CMOS photodiode array and held by using a thin polyurethane foam layer for compression between the screen and a 1-mm-thick graphite cover. During the measurements, the readout time was fixed at 550 ms.

RQA, which is the radiation quality based on addition of a certain amount of aluminum filtration, is one of the standard radiation qualities suggested by the IEC for the purpose of characterization of medical diagnostic X-ray equipment [15]. Among the various RQA series from 2 to 10, IEC 62220-1 [8] specifies four spectra such as RQA 3, 5, 7, and 9. If only one spectrum would be used, it should be RQA 5. Parameters for achieving the RQA 5 X-ray spectrum are the added filtration of 21 mm

of aluminum and an approximate X-ray tube voltage of 70 kV, which gives a nominal first half-value layer (HVL) of 7.1 mm in thickness of aluminum. In this study, we have obtained the HVL of 7.1 mm with the suggested parameters.

Although IEC 62220-1 recommends that the source-to-detector distance (SDD) should be at least 150 cm [8], the distance between the X-ray focal spot and the surface of the detector was set to 100 cm in this study, which was inevitable in the given experimental constraints. The added filtration was placed as close as possible to the source. The exposure rate at the entrance surface of the phosphor screen coupled to the CMOS photodiode array detector was measured by replacing it with a calibrated ion chamber (Victoreen 6000-528, Inovision, USA) while keeping the same distance.

C. Preprocessing of Image Data

Before obtaining the MTF and NPS, all the acquired images were corrected by offset and flat-field correction, which is a common procedure in digital X-ray imaging. In addition, the linearity of the detector system, which measures pixel values as a function of exposure, was verified by the measurement of characteristic curves. The worst case in linearity among six screens was the Lanex™ Fast Front screen, which showed a coefficient of determination of $R^2 = 0.97716$ in least-squares regression analysis with linear fit.

D. MTF

The MTF describes the resolving power of a detector. The MTF was measured using the slanted-slit method [16] to avoid aliasing due to the relatively large sampling pitch of the detector. This method can give us a finely sampled line-spread function (LSF) in which the sampling pitch might be much smaller than the inherent detector pixel pitch, d.

An image of a slit camera (I.I.E. GmbH, Aachen, Germany), with a slit width of 10 μm and placed at a slight angle, was obtained under the RQA 5 imaging condition. In order to correct for variations in X-ray intensity due to slight variations in slit width, pixel values perpendicular to the direction of the slit were normalized by dividing each pixel value by the sum of the pixel values in the selected row. Three transverse profiles along the length of the slit image data were then extracted and analyzed to determine the angle of the slit, θ, or the number of individual LSF, N, needed to obtain a finely sampled LSF [17]. Two crossing points in the profiles plot indicate the points at which the center of the slit is halfway between pixels, and the measurement of the distance in number of pixels between two points gives N. The slit image data were then rearranged for the synthesized LSF. Assuming a square pixel geometry of the detector, $N = 1/\tan \theta$ and the effective sampling pitch of the synthesized LSF, $d_{eff} = d/\tan \theta$. The MTF was computed by performing a fast Fourier transformation (FFT) of the synthesized LSF and normalizing its value to unity at zero spatial frequency.

E. NPS

The NPS measures the change in the noise amplitude as a function of spatial frequency and bridges the noise and spatial resolution properties in an image. The NPS was measured using

a 2D Fourier analysis for white images [18], [19]. For the easier evaluation of DQE, we actually measured a normalized NPS (NNPS) such that

$$\mathrm{NNPS}(f) = \frac{\mathrm{NPS}(f)}{\overline{q}^2 \times \overline{G}^2} \qquad (1)$$

where f is the spatial frequency, and $\overline{q}$ and $\overline{G}$ are the average photon fluence and detector system gain, respectively.

Assuming that the detector is ergodic, more than 100 images, each 128×128 pixels in size, were obtained by dividing a white image into half-overlapping sub-sections for several uniformly irradiated images. For each image, it is necessary to perform a detrending process to remove or reduce low-frequency trends such as long-range non-uniformity. A 2D second-order polynomial fit to each image and the subtraction of the polynomial fit from the corresponding image are often used. In this study, however, we subtracted instead the mean image value. The noise within each image was then converted to relative noise by dividing the image data by their mean value. The relative noise was squared and a 2D FFT was applied to compute NNPS. It is noted that the window-filtering process to reduce spectral leakage, normally performed before applying the FFT, was not considered in this study. Non-uniformity due to the slight difference among distances from the focal spot to a sub-section image was corrected by scaling the Fourier-transformed image data to a mean value of one at the reference position. The NNPS results were averaged to obtain the overall 2D NNPS. The 1D NNPS in the horizontal or vertical direction was obtained by averaging the directional frequency bands in the 2D NNPS near the selected central axis.

F. DQE

The DQE describes the transfer of signal-to-noise ratio (SNR) from the input to the output of a detector and thus measures the fraction of incident photon fluence contributing to the image quality. The DQE was assessed from the measured MTF, NPS and the estimated photon fluence

$$\mathrm{DQE}(f) = \frac{\overline{q} \times \overline{G}^2 \times \mathrm{MTF}^2(f)}{\mathrm{NPS}(f)} = \frac{\mathrm{MTF}^2(f)}{\overline{q} \times \mathrm{NNPS}(f)}. \qquad (2)$$

Assuming that the detector is an ideal photon-counting detector, the incident photon fluence $\overline{q}$ can be treated as the square of signal-to-noise ratio SNR^2. In actuality, the typical photodiode array is an integrating detector rather than a photon-counting device. However, the difference in SNR^2 between them is only a few percent [20].

The photon fluence was calculated using the experimentally measured exposure and HVL, and the computational program for X-ray spectral analysis. The program allows convenient calculation of X-ray spectra, filtration, and spectral characteristics such as mean photon energy, fluence, exposure, and HVL. The unattenuated spectra were integrated from the well-known empirical and semiempirical models [21]. For the given imaging conditions, the simulated X-ray spectrum was adjusted to agree with the HVL of 7.1 mm by slightly adjusting the intrinsic filtration and/or tuning the tube voltage.

Fig. 2 graphically illustrates the overall evaluation procedure of DQE including the measurements of MTF and NPS, and the estimation of the incident photon fluence based on the measurement of HVL and the X-ray spectral simulation.

III. RESULTS

A. MTF

Fig. 3 summarizes the measurement results of MTF for various screen types under the RQA 5 condition. The Min-R™ series show similar MTF results and the highest resolution. Lanex™ Medium and Fast Front screens show very similar but lower MTF performance. The Lanex™ Fast Back screen shows the lowest MTF. The Min-R™ series is optimized for mammography applications, and Lanex™ medium for chest radiography. The combination of Lanex™ Fast Front and Back screens is typically used for reduced dosage applications or for megavoltage portal imaging in radiation therapy. The measured results reflect these specific screen designs for the required imaging tasks.

The overall MTF of the detector system is affected by various physical parameters such as the X-ray focal spot size, the slit width, the magnification ratio, and the pixel size, and can be expressed as follows:

$$\mathrm{MTF}_{\mathrm{overall}}(f) = \mathrm{MTF}_{foc}(f) \times \mathrm{MTF}_{slit}(f) \\ \times \mathrm{MTF}_{\mathrm{pre}}(f) \times \mathrm{MTF}_{\mathrm{pix}}(f) \qquad (3)$$

where the subscripts foc, $slit$, and pix denote the focal spot, the slit width, and the pixel pitch of the CMOS photodiode array, respectively. The subscript pre indicates the presampling MTF of a screen as opposed to the sampled MTF which includes aliasing due to the effect of digital sampling. Since the SDD was set to 100 cm, which implies that we can make a parallel-beam approximation, and the slit camera was in contact with the entrance surface of the detector system, we can neglect the effect of the focal spot size. Due to the large SDD and the small height of the slit camera, we can also ignore the magnification of the slit width. Since the pixel pitch of the CMOS photodiode array is much larger than the slit width, the overall MTF can be approximated as

$$\mathrm{MTF}_{\mathrm{overall}}(f) \approx \mathrm{MTF}_{\mathrm{pre}}(f) \times \mathrm{MTF}_{\mathrm{pix}}(f). \qquad (4)$$

The theoretical MTF due to an aperture function can be expressed by the "sine cardinal" or simply "sinc" function. Assuming a square pixel geometry having a size of d in one direction

$$\mathrm{MTF}_{\mathrm{pix}}(f) = \mathrm{sinc}(\pi d f) = \frac{\sin(\pi d f)}{\pi d f} \qquad (5)$$

which is plotted in Fig. 3. We can note that the overall MTF is mostly determined by the resolving power of the screen itself. As a consequence, the resolving power of an indirect-detection digital imager employing a phosphor screen is mainly governed by the spreading of optical photons in the screen.
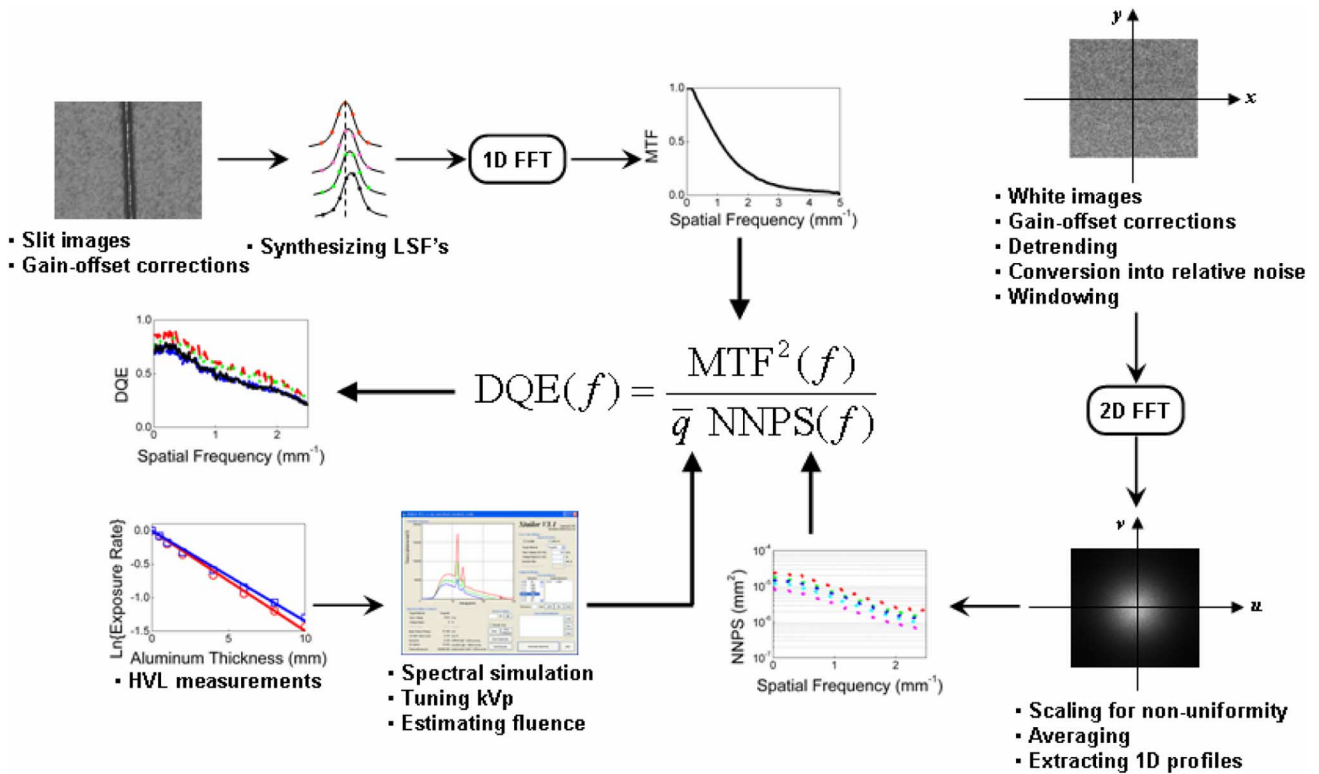
Fig. 2. Graphical illustration describing the evaluating procedure of DQE, which is based on the measured MTF, NPS, and the estimation of incident photon fluence. The detailed descriptions are given in the text.
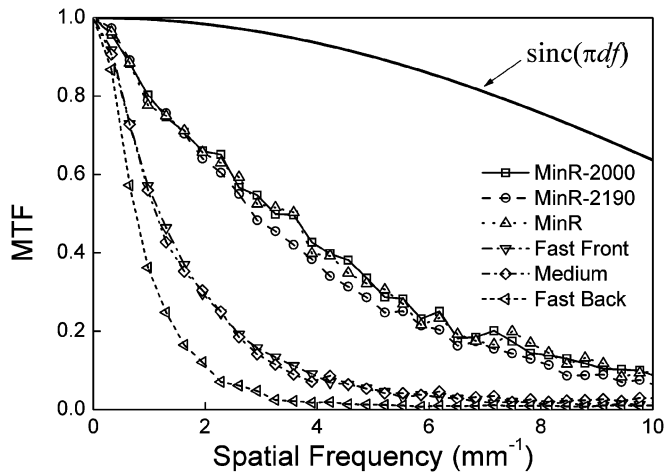

Fig. 3. Measured MTFs with the slanted-slit method. The theoretical MTF of the pixel pitch can be expressed as a sinc function, which is also plotted in this figure for the comparison.

Fig. 4. 2D plots of NNPS obtained for various screen types. The NPS pattern is symmetric.

B. NPS

Normalized noise-power spectra were calculated from white images obtained under the RQA 5 condition and an exposure of ~ 5 mR. 2D gray scale plots of the measured NNPSs are shown in Fig. 4, in which the axes *address* and *readout* indicate the electrical scanning and data transferring directions, respectively, in the CMOS photodiode array. All of the NNPS plots are symmetric around the zero-spatial-frequency point. We can also note the high spectral densities shown along the readout axis in the vicinity of the zero-spatial-frequency of the address axis.
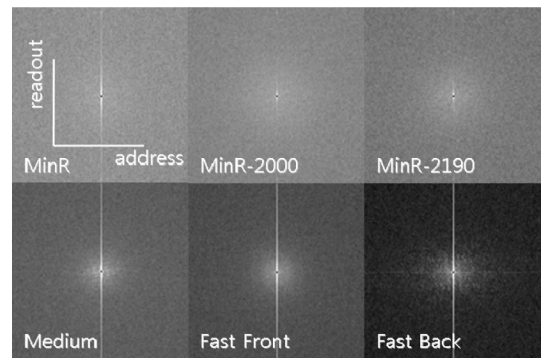
These are more apparently identified in Fig. 5, which plots the spectral density in three dimensions. We believe that this effect results from the readout process in the CMOS photodiode array, which would not be removed by the correction procedures.

Extracted 1D NNPSs are plotted in Fig. 6. The extraction was performed along the address axis avoiding the inclusion of the axis itself. The Min-R™ series screens show essentially white noise with respect to spatial frequency and significantly higher spectral densities compared with those of the other screens. The higher MTF performance might reflect this white-noise property in part. In a previous study, it was pointed out that in a detector employing a thin phosphor the extra noise due to the direct absorption of X-ray photons in the photodiode is white [22]. This additional white noise can further raise the spectral density in the high spatial frequency band. The proof that the NNPS due
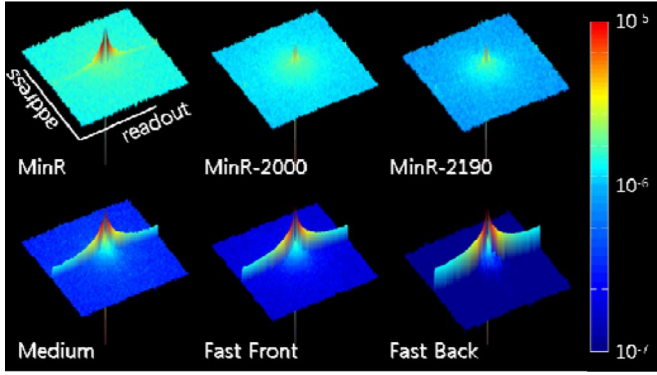
Fig. 5.   3D plots of NNPS obtained for various screen types. The normalized spectral density decreases as the screen thickness increases.
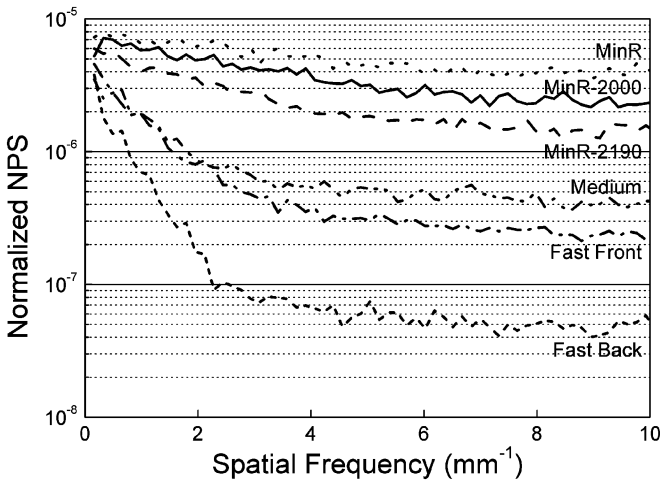

Fig. 6.   Extracted 1D NNPS profiles for various screen types. Min-R™ series screens show a white noise property.

Fig. 7.   Calculated DQEs for various screen types. Thick phosphor screens give a higher value of DQE below the spatial frequency of ~ 2 mm^{-1}. Thin phosphor screens preserve DQE even at higher spatial frequencies.

to the direct X-rays is white is shown in [23]. By contrast, the Lanex™ Fast Back screen shows a rapid decrease of spectral densities in the low spatial frequency band. This implies a statistical correlation of optical photons over long distances in this phosphor.

C. DQE

The DQE was calculated from (2). In order to match the spatial frequencies between the MTF and NNPS, a Lorenzian function was used to fit the MTF

$$\text{MTF}_{\text{pre}}(f) = \frac{1}{1 + k_L f^2} \qquad (6)$$

which describes a Fourier pair for the LSF expressed in exponential decay form. k_L is a fitting parameter describing the relative blur of the screen. Fig. 7 summarizes the plot of calculated DQE. As expected, the DQE of the Min-R™ series screens is lower below a spatial frequency of ~ 2 mm^{-1}, but decreases less rapidly at higher frequencies.

IV. DISCUSSION

The MTF is a good measure to compare the overall resolving power among several imaging systems. A spatial frequency cor-
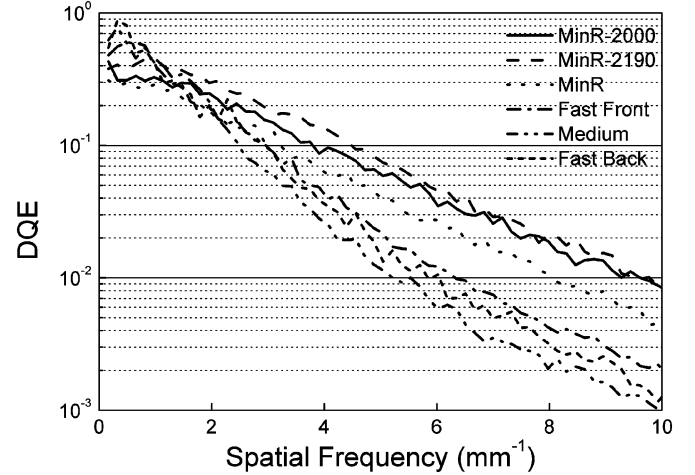
responding to an MTF of 10% is typically used to describe the system resolution with a single value, e.g., the distinguishable line pairs per millimeter or lp/mm. This originates from the definition of the Rayleigh diffraction limit in optics, in which the Rayleigh limit is equivalent to an MTF of $\sim 9\%$. To obtain a single-valued MTF descriptor, we instead propose the concept of an effective aperture having a dimension of length, because "length" rather than "lp/mm" is more intuitive when evaluating the spatial resolution of an imaging system.

From the definition of the effective aperture of Wagner *et al.* [24], we define an effective aperture in units of length

$$d_{eff} = \frac{1}{2 \times \text{BWI}} \qquad (7)$$

where the information bandwidth integral (BWI) is given by

$$\text{BWI} = \int_0^\infty \text{MTF}^2(f) df. \qquad (8)$$

If the experimental MTF is closely approximated by (6), the BWI can be expressed as a function of fitting parameter k_L so that $\text{BWI} = 2\sqrt{k_L/\pi}$. The derivation is given in the Appendix. As described in [24], the overall effective aperture can be calculated by the triangular addition law for each corresponding component

$$d_{\text{overall}} = \left[\sum_i d_i^2 \right]^{1/2} \qquad (9)$$

where the subscript i indicates a component giving rise to blurring and corresponds to *pre* and *pix* in this study.

Based on the calculated effective aperture and the measured sensitivity in units of digital signal (or analog-to-digital converted unit) per exposure (ADU/mR), we plotted tradeoff curves as shown in Fig. 8, which describes the competition between the sensitivity and spatial resolution of screens as a function of mass thickness. These figure-of-merit (FOM) curves will be useful to select an appropriate screen for a given imaging task when designing an indirect-detection imager.
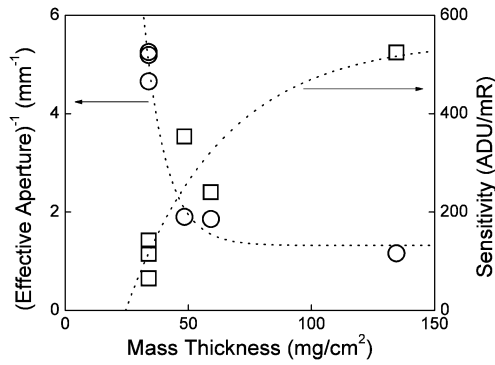
Fig. 8. Figure-of-merit curves describing the tradeoff between the spatial resolution and X-ray sensitivity as a function of screen mass thickness. The FOM provides an intuitive measure for selecting a screen in the design of an indirect-detection imager.

V. CONCLUSION

The selection or design of the Gd_2O_2S:Tb granular phosphor screen should be optimized with respect to the relevant imaging task. We believe that the measurement results obtained in this study, such as MTF, NPS, and DQE, will aid in the process of determining the design criteria for a digital X-ray imaging system with a Gd_2O_2S:Tb screen. As a single-valued MTF descriptor, the concept of effective aperture having a dimension of length, has been introduced. With the calculated effective apertures and the measured X-ray sensitivity, we have shown FOM curves as a function of screen mass thickness. This study is useful to design scintillator-based imaging detectors for a given imaging task.

APPENDIX

In this Appendix section, we show that the BWI of the experimental MTF expressed as a Lorenzian function converges.

Substituting (6) into (8), we then have

$$\text{BWI} = \int_0^\infty \frac{df}{(1 + k_L f^2)^2} = \frac{1}{k_L^2} \int_0^\infty \frac{df}{\left(\frac{1}{k_L} + f^2\right)^2}. \quad \text{(A1)}$$

Using the definite integral (for $0 < m + 1 < nr$) of

$$\int_0^\infty \frac{x^m}{(a^n + x^n)^r} dx = \frac{(-1)^{r-1} \pi a^{m+1-nr} \Gamma\left(\frac{m+1}{n}\right)}{n \sin\left\{\frac{(m+1)\pi}{n}\right\} (r-1)! \Gamma\left(\frac{m+1}{n}\right)} \quad \text{(A2)}$$

equation (A1) is simplified to

$$\text{BWI} = \frac{2\sqrt{k_L}}{\pi}. \quad \text{(A3)}$$

REFERENCES

[1] H. G. Chotas, J. T. Dobbins, III, and C. E. Ravin, "Principles of digital radiography with large-area, electronically readable detectors: A review of the basics," *Radiology*, vol. 210, pp. 595–599, 1999.

[2] H. K. Kim, G. Cho, S. W. Lee, Y. H. Shin, and H. S. Cho, "Development and evaluation of a digital radiographic system based on CMOS image sensor," *IEEE Trans. Nucl. Sci.*, vol. 48, no. 3, pp. 662–666, Jun. 2001.

[3] M. Bigas, E. Cabruja, J. Forest, and J. Salvi, "Review of CMOS image sensors," *Microelectron. J.*, vol. 37, pp. 433–451, 2006.

[4] H. K. Kim, J. K. Ahn, and G. Cho, "Development of a lens-coupled CMOS detector for an X-ray inspection system," *Nucl. Instrum. Meth. A*, vol. 545, pp. 210–216, 2005.

[5] J.-M. Kim, H. K. Kim, M. H. Cheong, M. K. Cho, C.-S. Shon, and C. H. Lim, "Investigation of scintillation screens for X-ray imaging," *Key Eng. Mater.*, vol. 321–323, pp. 1056–1059, 2006.

[6] P. F. Liaparinos, I. S. Kandarakis, D. A. Cavouras, H. B. Delis, and G. S. Panayiotakis, "Modeling granular phosphor screens by monte carlo methods," *Med. Phys.*, vol. 33, pp. 4502–4514, 2006.

[7] V. V. Nagarkar, T. K. Gupta, S. R. Miller, Y. Klugerman, M. R. Squillante, and G. Entine, "Structured CsI(Tl) scintillators for X-ray imaging applications," *IEEE Trans. Nucl. Sci.*, vol. 45, no. 3, pp. 492–496, Jun. 1998.

[8] Medical Electrical Equipment—Characteristics of Digital X-ray Imaging Devices—Part 1: Determination of the Detective Quantum Efficiency IEC, International Electrotechnical Commission, Geneva, Switzerland, 2003, IEC 62220-1.

[9] J. H. Siewerdsen, L. E. Antonuk, Y. El-Mohri, J. Yorkston, W. Huang, and I. A. Cunningham, "Signal, noise power spectrum, and detective quantum efficiency of indirect-detection flat-panel imagers for diagnostic radiology," *Med. Phys.*, vol. 25, pp. 614–628, 1998.

[10] A. L. Goertzen, V. Nagarkar, R. A. Street, M. J. Paulus, J. M. Boone, and S. R. Cherry, "A comparison of X-ray detectors for mouse CT imaging," *Phys. Med. Biol.*, vol. 49, pp. 5251–5265, 2004.

[11] E. Samei, "Image quality in two phosphor-based flat panel digital radiographic detectors," *Med. Phys.*, vol. 30, pp. 1747–1757, 2003.

[12] I. Kandarakis, D. Cavouras, G. S. Panayiotakis, D. Triantis, and C. D. Nomicos, "An experimental method for the determination of spatial-frequency-dependent detective quantum efficiency (DQE) of scintillators used in X-ray imaging detectors," *Nucl. Instrum. Meth. A*, vol. 399, pp. 335–342, 1997.

[13] D. J. Steklenski, *Private Communication*. Rochester, NY: Eastman Kodak Company, 1997.

[14] T. Graeve and G. Weckler, "High-resolution CMOS imaging detector," in *Proc. SPIE*, 2001, vol. 4320, pp. 68–75.

[15] Medical Diagnostic X-ray Equipment—Radiation Conditions for Sue in the Determination of Characteristics IEC, International Electrotechnical Commission, Geneva, Switzerland, 1994, IEC 61267.

[16] H. Fujita, D. Y. Tsai, T. Itoh, K. Doi, J. Morishita, K. Ueda, and A. Ohtsuka, "A simple method for determining the modulation transfer function in digital radiography," *IEEE Trans. Med. Imag.*, vol. 11, pp. 34–39, 1992.

[17] J. T. Dobbins, III, D. L. Ergun, L. Rutz, D. A. Hinshaw, H. Blume, and D. C. Clark, "DQE(f) of four generations of computed radiography acquisition devices," *Med. Phys.*, vol. 22, pp. 1581–1593, 1995.

[18] M. J. Flynn and E. Samei, "Experimental comparison of noise and resolution for $2k$ and $4k$ storage phosphor radiography systems," *Med. Phys.*, vol. 26, pp. 1612–1623, 1999.

[19] E. Samei and M. J. Flynn, "An experimental comparison of detector performance for direct and indirect digital radiography systems," *Med. Phys.*, vol. 30, pp. 608–622, 2003.

[20] K. Stierstorfer and M. Spahn, "Self-normalizing method to measure the detective quantum efficiency of a wide range of X-ray detectors," *Med. Phys.*, vol. 26, pp. 1312–1319, 1999.

[21] C.-S. Shon, H. K. Kim, M. K. Cho, M. H. Cheong, C. H. Lim, and J.-M. Kim, "Computational toolset for X-ray spectral analysis," *Key Eng. Mater.*, vol. 321–323, pp. 1060–1065, 2006.

[22] M. K. Cho, H. K. Kim, T. Graeve, and J.-M. Kim, "Characterization of CMOS pixel detectors for digital X-ray imaging," *Key Eng. Mater.*, vol. 321–323, pp. 1052–1055, 2006.

[23] H. K. Kim, "Generalized cascaded model to assess noise transfer in scintillator-based X-ray imaging detectors," *Appl. Phys. Lett.*, vol. 89, pp. 233504–233504, 2006.

[24] R. F. Wagner, K. E. Weaver, E. W. Denny, and R. G. Bostrom, "Toward a unified view of radiological imaging systems. Part I: Noiseless images," *Med. Phys.*, vol. 1, pp. 11–24, 1974.